Journal of Materials Science & Technology (2014).
30(11), 1145-1154.
DOI: http://dx.doi.org/10.1016/j.jmst.2014.08.008

Microstructural development and mechanical properties of PM Ti-45Al-2Nb-2Mn-0.8vol.%TiB_2 processed by Field Assisted Hot Pressing

R. Muñoz-Moreno[1, 2,*], E.M. Ruiz-Navas[1], B. Srinivasarao[2], J.M. Torralba[1,2]

[1] Department of Materials Science and Engineering, Universidad Carlos III de Madrid, Avda. Universidad 30, 28911 Leganés, Madrid, Spain

[2] IMDEA Materials Institute, C/Eric Kandel 2, 28906, Getafe, Madrid, Spain

*Corresponding author: rocio.munoz@imdea.org , Tel: +34 658 574 822, FAX: +34 915503047

ABSTRACT

A γ-TiAl intermetallic alloy, Ti-45Al-2Nb-2Mn(at.%)-0.8vol.%TiB_2, has been processed from gas atomized prealloyed powder by field assisted hot pressing (FAHP). An initial analysis of the prealloyed powder helped on the understanding of the intermetallic sintering behavior. Atomized powder consisted on α metastable phase that transformed into α_2+γ equilibrium phases by thermal treating. Different powder particle microstructures were found, which influence the microstructure development of the FAHP γ-TiAl material depending on the sintering temperature. Duplex, nearly lamellar and fully lamellar microstructures were obtained for the sintering temperatures above 1000 ºC. Lower consolidation temperatures, below 1000 ^{o}C, showed the formation of an Al rich phase at powder particle boundaries, which is deleterious to the mechanical properties. High compressive yield strength of 1050 MPa was observed in FAHP duplex microstructures samples at room temperature. Whereas nearly lamellar and fully lamellar microstructures showed yield strength values of 655 and 626 MPa at room temperature and 440 and 425 MPa at 750 ^{o}C respectively, which are superior when compared with similar alloys processed by other techniques. These excellent properties can be explained due to the different volume fractions of the α_2 and γ phases and the refinement of the PM microstructures.

Key words: titanium aluminides, powder metallurgy, microstructure, mechanical properties, field assisted sintering

1. INTRODUCTION

Titanium aluminides are important intermetallic alloys targeted for high temperature aerospace applications, namely the blades of low pressure turbines (LPT), because they can provide increased thrust-to-weight ratios and improved efficiency[1-4]. These blades must operate in aggressive environments at temperatures up to 750 ºC, where titanium aluminides possess reasonably good creep and oxidation behavior[5-7]. Therefore these alloys have the potential to replace the currently used heavier Ni-base superalloys.

Two main approaches are currently being used in order to optimize the microstructure and mechanical properties and they are by suitable alloy design and by choosing the proper processing route. Dual phase γ-TiAl alloys (γ-TiAl, tetragonal $L1_0$ structure and α_2-Ti_3Al, hexagonal DO_{19} structure) exhibit various microstructures consisting of different volume fractions of equiaxed grains and lamellar colonies. Depending on their microstructure, they are classified as duplex (comprising similar volume fractions of equiaxed grains and lamellar colonies), nearly lamellar (containing a small fraction of equiaxed grains) and fully lamellar (only composed by lamellar colonies). Lamellar microstructures make the material more resistant to creep conditions, while equiaxed grain microstructures are more ductile at room temperature[8, 9]. Even though, single phase γ-TiAl alloys possess better ductility due to $L1_0$ structure, they show strong plastic anisotropy, prone to embrittlement due to oxygen contamination and poor fatigue resistance[8]. Therefore, extensive research has been carried out in order to achieve a two phase/multi phase microstructure (consisting γ-TiAl, α_2-Ti_3Al and β/B2) by varying Al concentration in the range of 42 to 48 at.% and by other alloying additions such as Cr, Nb, W etc. The primary goal is to enhance the dislocation generation, thereby increasing the ductility (phase boundaries between γ and α_2), to scavenge the oxygen contamination (α/α_2), to increase the hot processing ability (β/B2) and to increase the creep and fatigue resistance (lamellar structure consisting of γ and α_2)[9, 10]. Apart from changing the phase transformation behavior, the alloying additions have other functional properties. For example, addition of Cr, Mn and V leads to an increase in ductility, while Nb, W, Mo and Ta increases

the high temperature oxidation resistance, creep resistance and high temperature strength. In addition, alloying with B leads to a microstructure refinement[11, 12]. Many studies has been reported, showing the possibility to tune the microstructure and mechanical properties with a combination and differing amounts of these elements[12-16].

The most popular processing routes that have been explored so far are a combination of casting, thermomechanical and/or heat treatments and powder metallurgy (PM)[15, 17-20]. Even though, casting is the best established process, it suffers from several drawbacks such as choosing proper composition in order obtain good melt fluidity, casting defects, segregation of alloying elements, poor workability, need for post consolidation, heat treatments, etc[19, 21]. To overcome some of these drawbacks several new techniques such as counter-gravity and centrifugal casting techniques have been developed, even then these techniques heavily depends on the prior knowledge of the equilibrium phase diagram and further optimization of heat treatments[15]. Compared to the casting route, PM offers several advantages such as refining the microstructure, improving structural and chemical homogeneity and providing freedom of choosing composition and initial raw materials, reducing the need to separate heat treatments and directly obtaining final product shape requiring minimal post processing treatments. Particularly, a wide variety of powder metallurgy routes have been considered to develop γ-TiAl intermetallics. Starting from prealloyed powder benefits the microstructural homogenization and the mechanical properties. Prealloyed powder could be obtained by different gas atomization techniques, such as plasma inert-gas atomization (PIGA), titanium gas-atomizer process (TGA) or electrode induction gas atomization (EIGA) among others[22]. They will define the powder characteristics and so the final sintered material properties. Since the prealloyed TiAl powder particles present a significant hardness, cold compaction is replaced with hot consolidation techniques. In addition, the processing time can be reduced by using newer techniques known as field activated sintering (e.g., spark plasma sintering) where simultaneous application of pressure and pulsed/continuous direct/alternating current is used[23, 24]. It has been found that the effect of the current is the fast generation of internal heat by Joule

effect which increases the sintering kinetics[25, 26], providing a rapid densification of powders and minimal grain growth. Extensive research is currently going on to process various compositions, to understand microstructure evolution, mechanical properties and upscaling to produce actual components by using field activated sintering techniques[14, 19, 27-36].

In the current work, a commercial Ti-45Al-2Nb-2Mn(at.%)-0.8 vol.% TiB_2 prealloyed powder has been sintered using one of the field activated sintering techniques known as field assisted hot pressing (FAHP), where simultaneous application of pressure and continuous alternating current is used. Different sintering temperatures have been selected to understand the microstructure development. Finally corresponding mechanical properties at room and elevated temperatures have been discussed.

2. EXPERIMENTAL

Prealloyed powder (Ti-45Al-2Nb-2Mn(at.%)-0.8vol.%TiB_2) was employed as a raw material for the FAHP. The powder was gas atomized by EIGA at Helmholtz-Zentrum für Material und Küstenforschung GmbH (Geesthacht, Germany)[22, 37]. Powder size distribution was measured by a Mastersizer 2000 (Malvern, United Kingdom). X-ray diffraction (XRD) at room temperature was performed in a Philips Panalytical X'pert PRO MRD system (Almelo, The Netherlands) and intensity versus 2θ plots was acquired. In addition, the as-received prealloyed powder was analyzed by means of high temperature XRD at 600 ºC, 800 ºC and 1000 ºC. High temperature XRD was performed by a X-ray diffractometer Philips Panalytical X'Pert PRO MPD (Almelo, The Netherlands), fitted with a temperature chamber Anton Paar HTK 1200 (Graz, Austria). The microstructure analysis was done using a scanning electron microscope (SEM), Zeiss (Jena, Germany) EVO MA15 equipped with an Energy Dispersive Spectroscopy (EDS) system (Oxford INCA x-act). Differential thermal analysis (DTA) was performed on a Setsys Evolution TGA & DTA/DSC (Setaram, France).

FAHP specimens were manufactured in a Gleeble 3800 equipment (Dynamic Systems Inc., USA), which allows physical simulation processing of materials. In this case it was used to perform the pressing and sintering steps simultaneously, by applying a continuous low

frequency alternate current to heat the material by Joule effect. The prealloyed powder was poured into a cylindrical graphite die having an internal diameter of 10 mm for the consolidation. An outside view of the Gleeble vacuum chamber with the gripped graphite die used for the processing is described in a previous work[38]. During processing the temperatures were registered in the two punches and at the center of the die, where the thermocouple was placed at 1 mm above the sample surface. Initially, the graphite die was gripped at a load of 5 MPa inside the vacuum chamber and once the degassing temperature is overcome, the pressure is increased to 50 MPa. By observing the vacuum pressure, it was established that the degassing was stabilized at temperatures above 200 ºC. The γ-TiAl alloy has been processed by FAHP for a period of 2 to10 minutes at different temperatures. The conditions were: FAHP1, 900 ºC - 10 min; FAHP2, 1000 ºC - 10 min; FAHP3, 1100 ºC - 10min; FAHP4, 1250 ºC - 10 min; FAHP5, 1350 ºC - 2 min. The heating rate was always 100 ºC/min, while the cooling rate registered was of 140 ºC/min. Density of the consolidated samples was studied using Archimedes method.

Microstructural analysis of the FAHP samples was carried out by the equipments detailed previously and with transmission electron microscopy (TEM). TEM analysis was performed using a FEI Instruments (Oregon, USA) Tecnai T20 TEM at 200 kV. The TEM foils were prepared by polishing the samples to a thickness of approximately 200 µm, then punching 3 mm diameter disks, and finally thinning them using a Struers (Ballerup, Denmark) twinjet Tenupol-5 electropolisher until perforation. The electropolishing solution, which consisted of 5% perchloric acid, 35% butanol, 60% methanol, was held at a constant temperature of -30 ºC and the voltage for sample preparation was 40V.

Compression tests of the processed samples were performed under a constant strain rate of 10^{-3} s^{-1} in vacuum at room temperature and at 750 ºC in a Gleeble 3800 equipment. Compression samples had a cylindrical geometry with a length of 4.5 mm and a diameter of 3 mm. For high temperature tests, heating was programmed to be 10 ºC/min and a soaking time of 1 minute was used after reaching 750 ºC. Changing the soaking time to 10 min did not resulted in any significant change in the mechanical properties. Nanoindentation analysis was carried out

using a TI950 Triboindenter™ (Hysitron, Inc., Minneapolis, MN) and measurements were done under a constant load of 12 mN.

3. RESULTS AND DISCUSSION

3.1 Powder characterization

Figure 1 shows the powder particle size distribution and the SEM micrographs of the powder showing its spherical morphology. The average particle size was of 51 μm and the particle sizes measured at 10, 50 and 90% of the total volume of the sample were 17.3, 51.2 and 117.8 μm respectively (Fig. 1a). As can be observed in Figure 1b-c, depending on the particle size, different powder microstructures are identified. It is a consequence of the size influence on the solidification rate at a constant cooling rate[22]. Small particles (<50 μm) (Fig. 1b), have a microstructure composed by a major volume fraction of dendritic and equiaxed grain morphologies, surrounded by a darker interdendritic regions and bright ribbons. However, bigger particles (>50 μm) (Fig. 1c), have a microstructure composed by dendrites that in some areas have grown into single and cluster of large grains, due to the lower solidification rates. In large particles, interdendritic channels with bright ribbons were also observed. In addition, brighter single phase regions are observed randomly inside the particles of different sizes (Fig. 1d) and they are composed by subgrains (Fig. 1e). The reason for the difference in varying microstructure contrast can be understood by studying the partitioning of different alloying elements in the dendrites and interdendritic regions. Literature analysis indicates that the solubility of Mn in α -Ti is lower compared to Nb[39-41]. EDX analysis confirmed that a lower Mn and a higher Nb concentration were present in the single phase and dendritic regions resulting in the brighter contrast of these areas. Whereas, EDX analysis carried out at the interdendritic areas indicated a higher Al and Mn concentration consistent with the dark contrast. The bright ribbons are associated with the titanium borides as they are easily distinguished by their lacey morphology[42]. Regarding the relationship between the powder cooling rate and the microstructure, similar characteristics have been reported by Yang *et al*. [43].

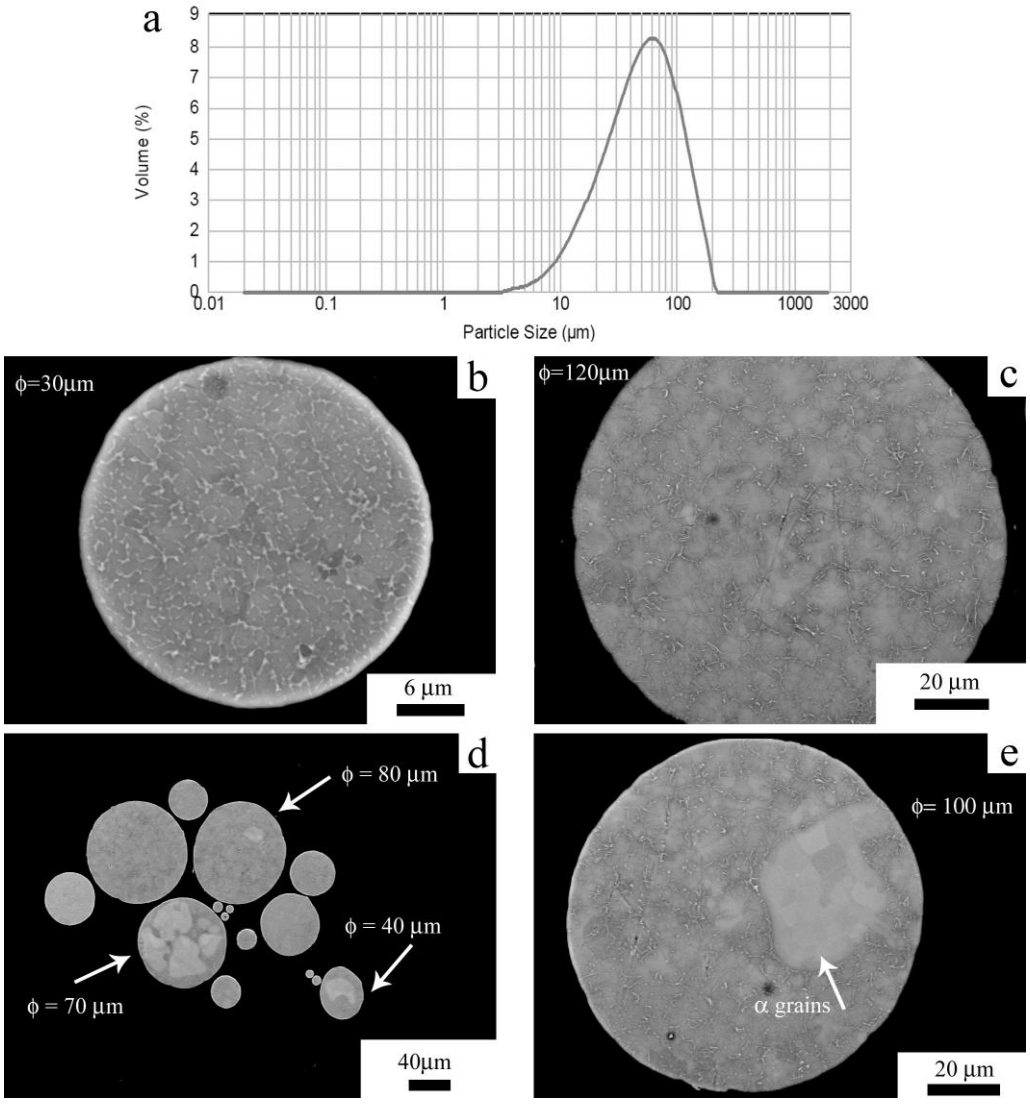

Fig. 1 (a) Powder particle size distribution and (b-e) backscattered (BSE) SEM micrographs showing the prealloyed powder microstructures for different particle's size: (a) 30 μm diameter and (b) 120 μm diameter; (c, d) single phase regions present in particles of different sizes

The XRD pattern at room temperature of the as-received prealloyed powder (Fig. 2) shows that the material mainly contains α-Ti_3Al phase (a=2.8175 *Å*; c=4.6100 *Å*), which is consistent with the microstructures above mentioned (Fig. 1e). The absence of the superlattice peak (2θ=26.2º) confirms that it does not correspond to the α_2 stable phase. The cooling rate reached during EIGA process is ~10^5 K/s, which is slightly lower in comparison to rapid solidification process but higher than the conventional gas atomization[22]. Therefore, this cooling rate justifies the alloying elements and micro-constituents distribution observed in these microstructures, as well as, the detected α metastable phase and the absence of γ phase peaks. It

is speculated that the interdendritic regions with a high amount of Al concentration might corresponds to γ-phase but because the volume fraction is very small and the main peak is very close to the α-phase, it is difficult to detect in the current XRD profile.

DTA analysis of the powder was done and compared with those of identical composition of (Ti-45Al-2Nb-2Mn (at.%)-0.8vol.%TiB_2) centrifugally-cast sample (Fig. 3). From the DTA of the centrifugally cast alloy, the phase transformation temperatures were identified and considered as reference: $T_{eutectoid}$= 1150 ºC, $T_{\alpha\ transus}$= 1290 ºC, $T_{melting}$= 1490 ºC. Comparing the powder and the as-cast DTA, it was observed that the thermal behavior was similar except for the range of temperatures between 600 ºC to 750 ºC (Fig. 3). In order to understand the transformations happening in the powder at these temperatures, high temperature XRD was performed at 600 ºC, 800 ºC and 1000 ºC and compared with the as-received powder XRD profile (Fig. 2). The XRD pattern obtained from the powder at 600 ºC shows a decrease in the intensities of the α peaks. Increasing the temperature to 800 °C leads to a greater decrease of α peaks combined with the appearance of γ-TiAl and α_2-Ti_3Al peaks, suggesting that the α metastable phase started to transform into α_2+γ at around this temperature. Finally, at the highest temperature (1000 ºC), the transformation is completed and α_2+γ peak intensities are higher and clearly recognizable. Therefore, in order to achieve a complete transformation during consolidation of the previous α metastable powder, the sintering temperature must be equal or greater than 1000 °C.

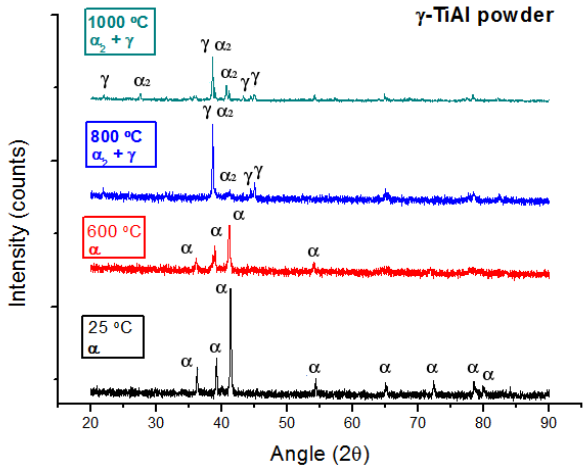

Fig. 2 XRD patterns of prealloyed Ti-45Al-2 Nb-2 Mn-0.8vol.%TiB_2 powder at 25 ºC, 600 ºC, 800 ºC and 1000 ºC

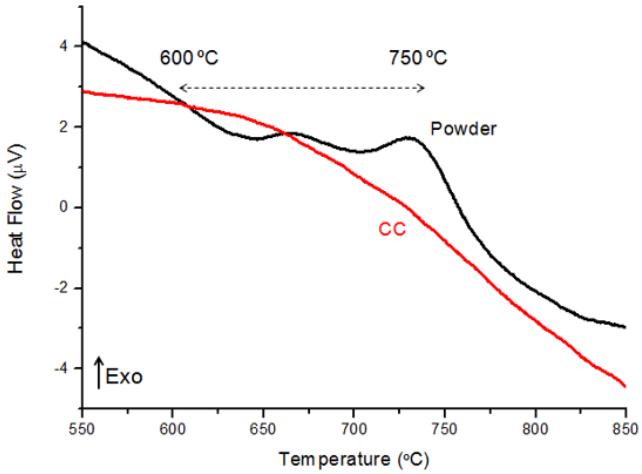

Fig. 3 DTA analysis comparing the powder and the centrifugally cast Ti-45Al-2Nb-2Mn-0.8vol.%TiB_2 alloy showing different thermal behavior at 600 ºC - 750 ºC

The DTA analysis and the high temperature XRD patterns show consistent results. Transformations observed at 600-750 ºC in the DTA can be associated to those identified in the high temperature XRD. It seems that once the metastable powder is heated to temperatures above 800 ºC, stable γ phase appears and rising the temperatures leads to the stabilization of α_2+γ phases, according to the equilibrium phase diagram[26,33,44,45]. However, as Figure 4 shows, heating the metastable powder to 800 ºC in the DTA and cooling, is not enough to form lamellar structures consisting of α_2+γ phases. Therefore, either longer times or higher temperatures are necessary.

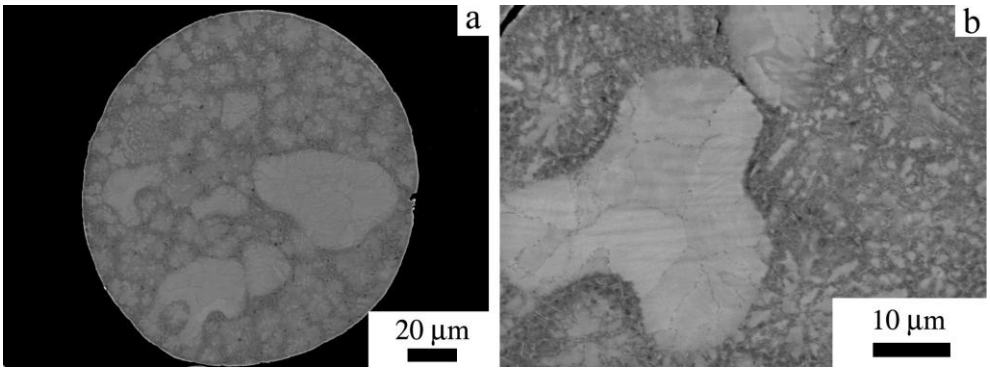

Fig. 4 BSE SEM micrographs (a) at low and (b) high magnification of the powder heated at 800 ºC.

3.2 FAHP γ-TiAl consolidation

The γ-TiAl prealloyed powder was processed by FAHP at the five different conditions detailed above. Figure 5 shows two representative curves illustrating the typical evolution of the temperature and displacement with respect to time recorded during the consolidation. From the punch displacement it can be observed that, for consolidation at temperatures around 900 ºC, the main densification must be reached during the first 5 minutes of the dwell (Fig. 5a). However, for higher processing temperatures (Fig. 5b) the displacement reveals a swelling and it could be interpreted as a result of the system dilatation[29]. The relative densities of the consolidated samples were found to be higher than 99% for all the processing conditions.

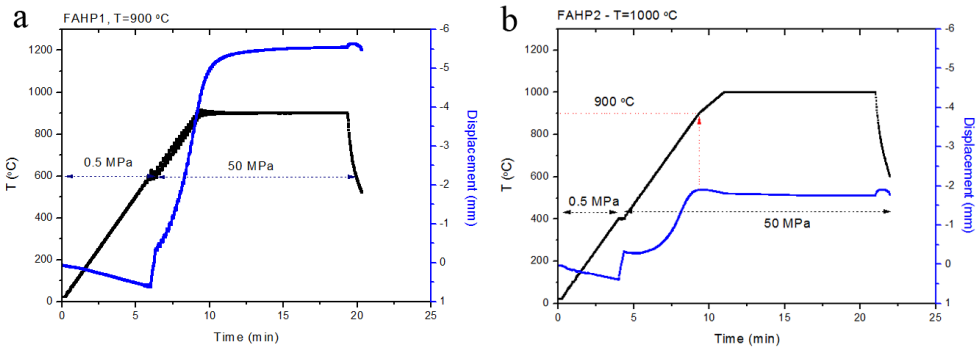

Fig. 5 Typical evolution of the temperature and displacement versus time recorded in-situ during the FAHP processing at (a) 900 °C and at (b) 1000 °C during 10 minutes

The XRD patterns corresponding to the FAHP materials (Fig. 6) show the presence α_2 and γ phases after consolidation at all the studied sintering temperatures and times. At higher processing temperatures, $\alpha_2+\gamma$ peaks become more intense and defined. Therefore, for all consolidation conditions, the metastable powder is transformed into $\alpha_2+\gamma$ phases and their volume fraction vary depending on the sintering condition, which is consistent with the high temperature XRD observations (Fig. 2).

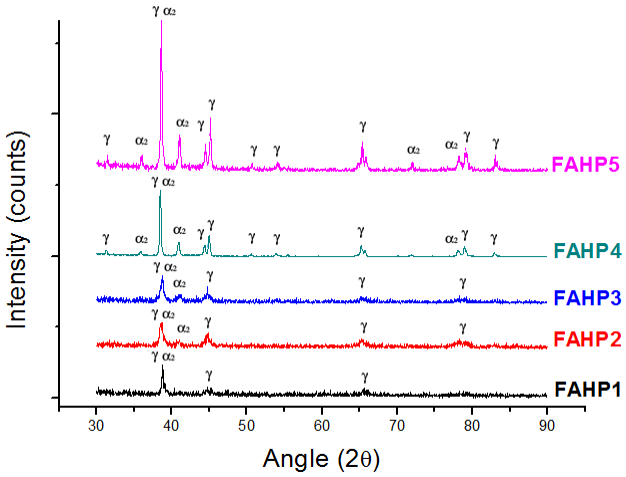

Fig. 6 XRD patterns of FAHP1, FAHP2, FAHP3, FAHP4 and FAHP5 materials exhibiting α_2+γ peaks.

Figure 7 shows BSE SEM micrographs of the material processed at 900 ºC (FAHP1) at various locations of the sintered compact. The micrographs at the center as well as at near the edge shows a clear heritage of the former powder particle boundaries (Fig. 7a, c). Particularly, in the center of the sample a duplex microstructure can be recognized (Fig. 7b). Then, the metastable and heterogeneous microstructure present in the as-received powder particles starts to transform into the equilibrium phases and homogenize by diffusion at 900 ºC. Moreover, Figure 7b shows the former single phase regions transformed into equilibrium lamellar colonies consisting of α_2 and γ phases. The different lamellae orientations correspond to the former equiaxed subgrains orientation identified in the single phase areas of the as-received powder (Fig. 1e). It is well known, that an increasing of the processing temperature in these alloys entails a stabilization of α regions. Moreover, the consolidation of the intermetallic alloy at regions closer to the α-phase field promotes the formation of lamellar microstructures[45-49]. Therefore, in the processing of FAHP1, lamellar microstructures first appear in the higher concentration α retained single phase regions. However, the lamellar colonies are surrounded by a high amount of equiaxed grains because the processing temperature might not be high enough to go through the eutectoid transformation and stabilize the α phase field.

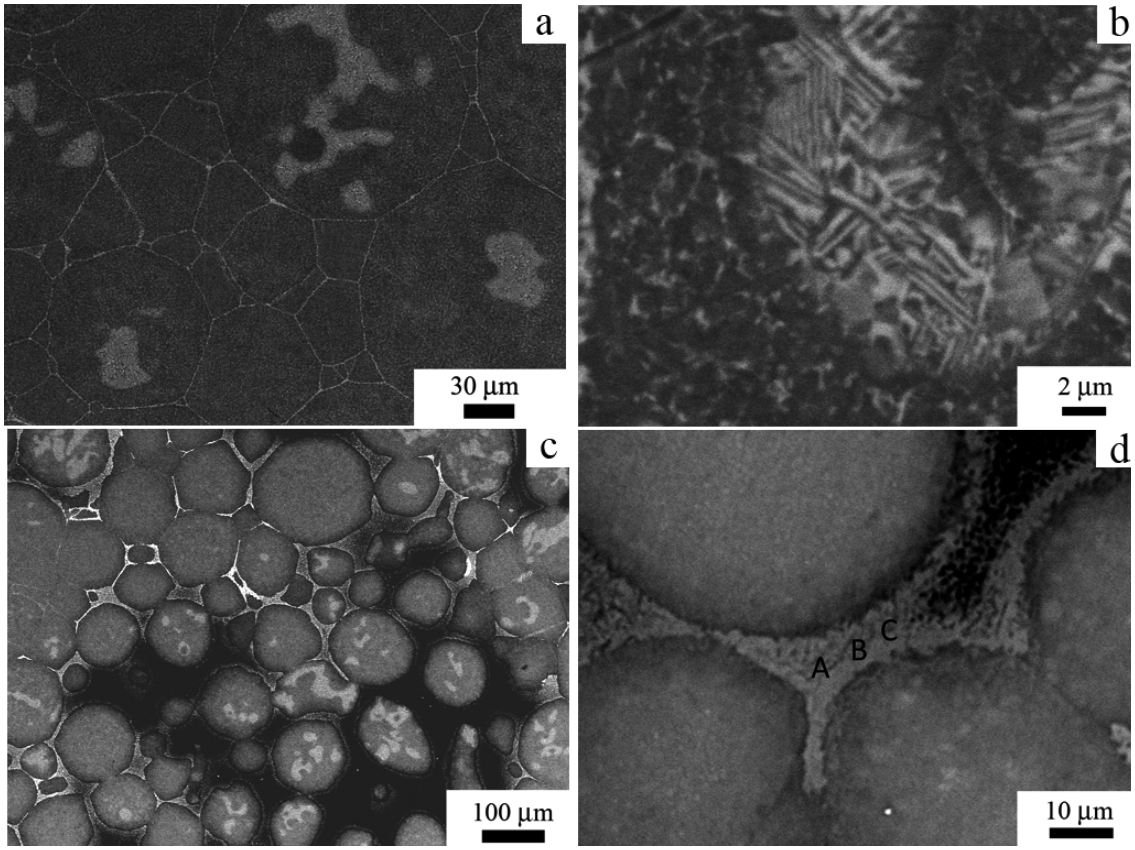

Fig. 7 BSE SEM micrographs showing the microstructure of the FAHP1 consolidated sample: (a-b) duplex microstructure in the center of the sample, (c) not completely sintered edge area and (d) Al_3Ti phase boundary area between the powder particles of FAHP1 sample.

In FAHP1 the densification is complete in the center, whereas a high concentration of pores are located near the edges (Fig. 7c), where the temperature measured by the die's thermocouple was of T_{FAHP1}=900 ºC. It evidences a gradient of the temperature in the radial direction of the sample. Then, the optimum sintering temperature is not reached in the edges since the powder densification is just starting at this temperature and poor diffusion phenomenon has taken place in this area. However, the optimum densification in the center of the sample reveals an increase in the measured T_{FAHP1}. This gradient in temperature has also been reported and modeled by other authors for similar hot consolidation processes such as spark plasma sintering[25, 45]. Figure 7c shows evidences of sintering and densification by the formation of sintering necks between particles. In particular, a close up view of these powder particle boundaries situated near the edge of the sample is shown in Figure 7d. The EDX analysis taken from points A, B and C was found to be 72-75%Al, 23-25% Ti, 1-2%Nb, 1%

Mn, indicating that the phase formed at this location is close to Al_3Ti phase. In the field activated sintering processes the particle boundaries experience highest temperatures due to the generation of sparks or due to the high resistance for the current path and if sufficient time is employed mass transport takes place either by surface, grain boundary or volume diffusion. As the diffusion coefficient of Al in Ti and TiAl intermetallic is higher than that of Ti and other alloying elements[39], the elemental segregation to the particles surfaces can take place and promote the formation of Al enriched areas. The presence of interdendritic regions in the original powder particles with high concentration of Al could also serve as a source.

The gradient in density was not observed when the material was processed at 1000 ºC (FAHP2). BSE SEM micrographs in Figure 8a,b show the duplex microstructure, composed by equiaxed grains and lamellar colonies along the whole sample. The lamellar colony average size was of 23 μm. No pores or elemental segregation were observed throughout the sample. It suggests that processing at and above 1000 ºC allows a proper consolidation of the γ-TiAl alloy since the densification stage is well developed along the whole sample. A general view of this microstructure (Fig. 8a) still evidences the former powder particles and a microstructure similar to that observed in the center of the FAHP1 sample (Fig. 7a). In this condition, a gradient in the microstructure was not observed suggesting that when sintering was performed at 1000 ºC the entire sample was processed in the same phase field, below the eutectoid transformation[45-49]. Therefore, sintering at T>900ºC and below the eutectoid point promotes a complete densification of the material with a duplex microstructure.

A nearly lamellar microstructure can be recognized in the center of the sample processed at 1100 ºC (FAHP3) (Figs. 9a-b). However, a radial gradient in the microstructure was again observed with a transition from nearly lamellar in the center (right in Fig. 9c) to duplex in the edge (left in Fig. 9c). A good distribution of the alloying elements is confirmed by EDS in these transition areas. In this case, the gradient in the microstructure morphology along the sample's radial direction might be associated to the stability of the phases. As previously mentioned, according to the processing at different regions of the phase diagram, different microstructures

will be formed[45-49]. Therefore, during the FAHP3 processing, the real temperature of the material in the center of the sample might be higher and above the eutectoid point since higher volume fraction of lamellar colonies and no signs of former powder particles can be observed. However, in the edge of the sample, the sintering temperature (T_{FAHP3}=1100 ºC) is below the eutectoid point and a duplex microstructure is recognized as occurred with FAHP1 and FAHP2.

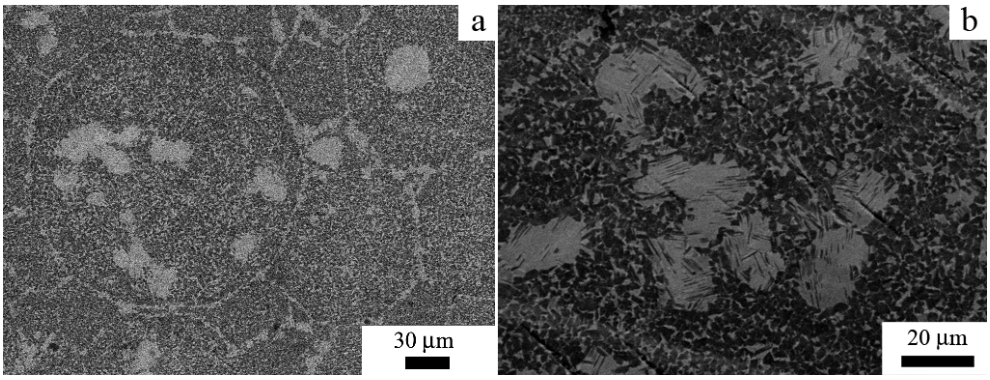

Fig. 8 BSE SEM micrographs showing the duplex microstructure of the FAHP2 consolidated sample (a) with signs of former powder particles and (b) a combination of lamellar colonies and equiaxed grains.

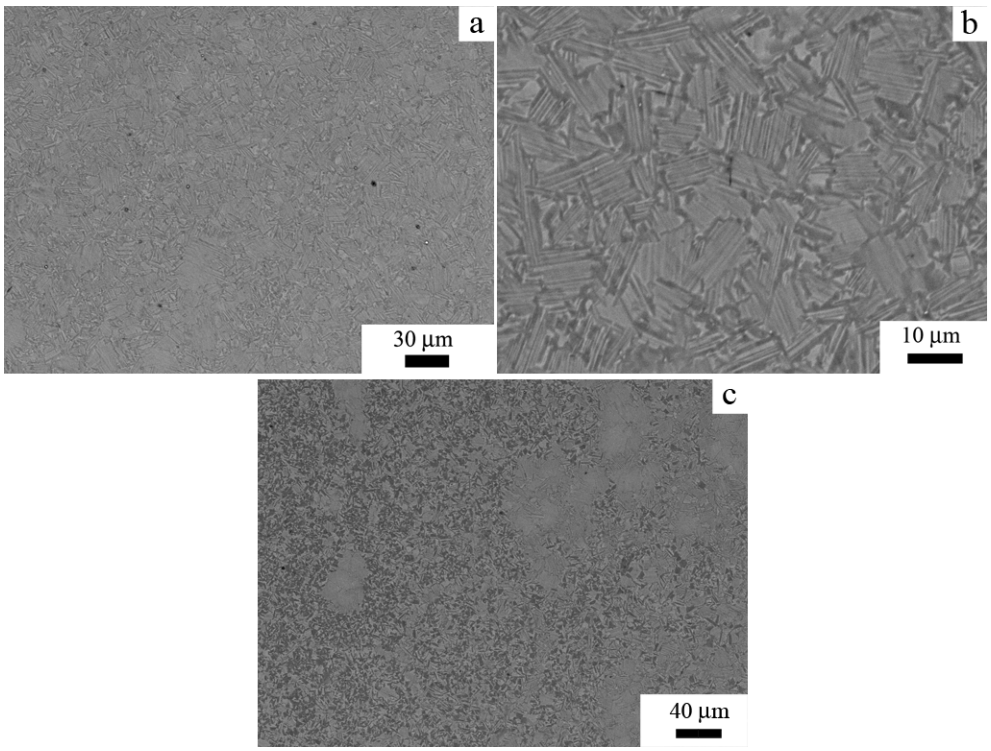

Fig. 9 BSE SEM micrographs showing the FAHP3 (a, b) nearly lamellar microstructure in the center of the sample and (c) the gradient in the microstructure along the sample's edges

After processing the intermetallic at 1250 ºC (FAHP4), a nearly lamellar microstructure was found along the whole sample (Figs. 10a-c) with a refined lamellar colony size of 9 μm. Since the processing temperature is above the eutectoid point, $\alpha_2+\gamma$ phases will precipitate from $\alpha+\gamma$ phases following the equilibrium phase diagram and forming nearly lamellar microstructures[45-49]. However, a small increase in the volume fraction of equiaxed grains was found in the edge (Fig. 10c) in comparison to the center (Figs.10a,b). It suggests that in the center area of the sample, transformations start at temperatures closer to the α-transus, a more stable condition for the lamellar structure formation. Figure 11 shows a TEM micrograph from the typical fine lamellar colony processed at 1250 ºC illustrating a lamellar width of 100 - 300 nm. Finally, processing at 1350 ºC (FAHP5), fully lamellar microstructures were obtained (Fig. 10d,e) with a coarser lamellar colony size of 27 μm. It confirms that processing at temperatures above the α–transus helps to obtain microstructures completely composed by lamellar colonies and that increasing processing temperatures also leads to a growth in the average colony size. Nevertheless, as it has been observed in all the processed samples, the average lamellar colony sizes reached thanks to the fast cooling rate provided by FAHP are significantly lower than those obtained by conventional casting[50]. In addition, brighter areas were found in FAHP5 material within the lamellar structure. These brighter areas, associated to heavier elements, might be related to possible retained β-phase as could be reached during these higher temperature conditions[51]. However, not significant predominance of β-phase is recognized as it is not identified in the corresponding XRD pattern (Fig. 6).

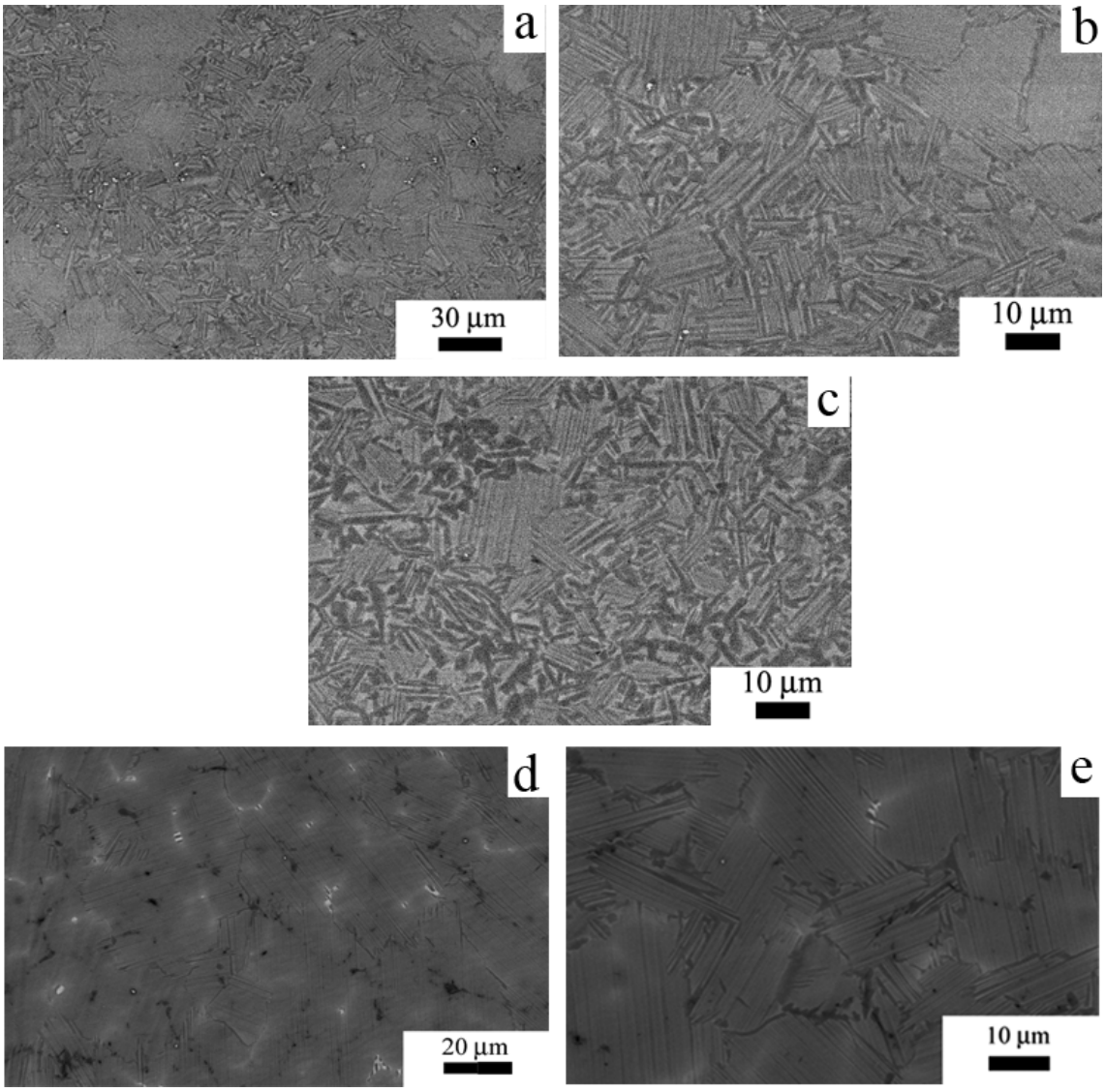

Fig. 10 BSE SEM micrographs showing the FAHP4 (a-b) nearly lamellar microstructure along the whole of the sample and (c) edges areas with an increasing of the equiaxed grains volume fraction; FAHP5 (d, e) fully lamellar microstructure

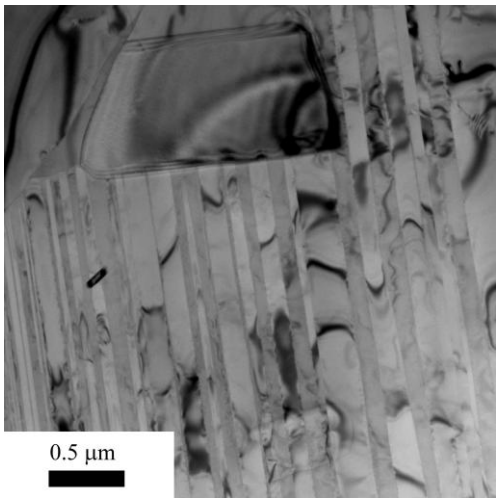

Fig. 11 TEM micrograph of the FAHP4 sample showing a fine lamellar colony

3.3 FAHP γ-TiAl material mechanical behavior

Duplex (FAHP2), nearly lamellar (FAHP4) and fully lamellar (FAHP5) microstructures were selected to analyze their mechanical behavior. Compression tests were carried out in these materials and its corresponding stress-strain curves are showed in Figure 12 for room temperature and high temperature (750 ºC) conditions. The yield strength values obtained at room temperature and high temperature for the FAHP2, FAHP4 and FAHP5 are 1058, 655, 626 and 303, 440 and 425 MPa respectively. As expected, at room temperature tests higher yield points were obtained for the lowest processing temperature material (FAHP2), while the materials processed at higher temperatures (FAHP4, FAHP5) showed lower yield point values (Fig. 12a). Particularly, FAHP4, with a lower colony size average (10 μm), exhibited higher yield point than FAHP5, with a higher colony size average (27 μm). Therefore, as previously reported, duplex microstructures present higher strength than lamellar ones at room temperature compression conditions[9]. Yield points of FAHP materials resulted higher yield point values than those obtained through SPS processing at higher processing temperatures with similar alloy compositions and microstructures[29, 36]. For example, room temperature tensile tests of these reported works are as follows: a yield stress of 432 MPa for a Ti-48Al-2Cr-2Nb duplex alloy[36] and of 445 MPa for a Ti-47Al-2Cr-2Nb lamellar alloy[29]. In addition, other PM processing of similar alloys reported lower yield stresses values. That is the case of a Ti-48Al-2Nb-2Mn duplex alloy processed by EBM (electron beam melting) with a yield stress of 350 MPa[52] and a Ti-45Al-2Nb-2Mn lamellar alloy processed by HIP with a yield stress of 471 MPa[53]. However, FAHP2 duplex microstructures showed lower elongation-to-failure. This inferior strain values can be associated to the initial drop on its stress-strain FAHP2 curve (Figure 12a) that might be due to an initial fracture of the more brittle Al_3Ti phase that keeps surrounding powder particles during densification at 900 ºC, as previously explained. Similar phenomenon has been also reported in other SPS research works with Al and Fe[54, 55], where depending on the phases present at the particle boundaries, the material exhibits either early failure or exhibit strain hardening resulting in greater ductility. Therefore, higher elongation-to-fracture might be

expected if avoiding the more brittle phase in the particles boundaries, due to the fine FAHP2 duplex microstructure. The effect of the Al_3Ti phase present at the particle boundaries on the mechanical properties is more visible when the compression tests were carried out at high temperatures. As shown in Figure 12b, before the yield point, the FAHP2 curve exhibits two slopes and the second slope varies in other samples tested at this condition. This is due to the different percentages of the Al_3Ti phase. In the case of lamellar microstructures, FAHP4 exhibited again higher yield point than FAHP5, which might be related to its inherent refined microstructure. Similar to the room temperature yield strength values, the high temperature ones also exhibit superior to some of the reported ingot alloys (100-260 MPa, Ti-42Al-8Nb-0.2W-0.1Y)[55]. Even though the current processing conditions on the Ti-45Al-2Nb-2Mn-0.8vol% TiB_2 alloy show excellent mechanical properties when compared to other alloys, the literature also indicates even better properties. Those instances are either due to the further refinement of the microstructure such as by mechanically milling/alloying processed alloys[32, 35] or when controlled heat treatments were applied[21].

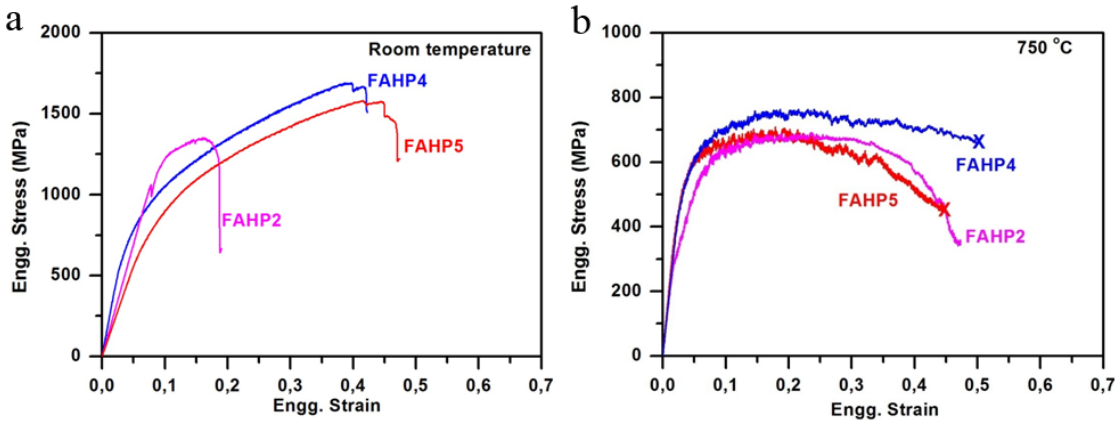

Fig. 12 Compression tests stress-strain curves at (a) room temperature and (b) high temperature (750 ºC) conditions for FAHP2, FAHP4 and FAHP5 materials. X indicates that the test is stopped

In order to establish the influence of the different microconstituents on the mechanical behavior, nanoindentation measurements were performed separately in the grains and in the colonies of a duplex microstructure (FAHP2). Figure 13 shows differences observed in reduced modulus values between the grains and the colonies. This different behavior can be associated with a predominance of different phases present. According to the theory, the elastic modulus values of α_2 and γ phases are $E(\alpha_2)$=146 GPa and $E(\gamma)$=172 GPa respectively[9], indicating that in the FAHP2 material the grain areas were mainly composed by γ phase and colony areas by α_2 phase, which fully confirms the above microstructural analysis.

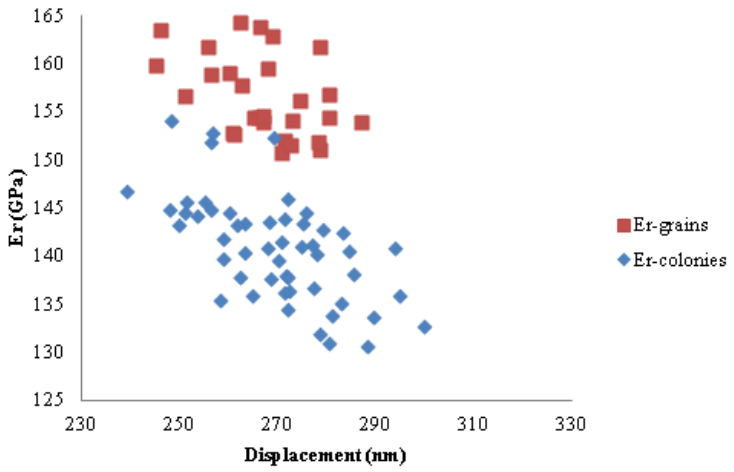

Fig. 13 Reduced modulus values of the different microconstituents obtained through nanoindentantion in the duplex (FAHP2) material

The results obtained from this research work show that FAHP materials can be manufactured through an optimal microstructural control which can give the opportunity to develop appropriate microstructures depending on its application.

4. SUMMARY

A γ-TiAl (Ti-45Al-2Nb-2Mn(at.%)-0.8vol.%TiB_2) intermetallic alloy has been processed by field assisted hot pressing, where simultaneous pressure and continuous alternating current were applied. The effect of the processing temperature was analyzed in order to understand the consolidation of the material and the phase transformations involved. In addition, the corresponding mechanical properties were analyzed. The following conclusions can be derived from the present study:

1. Prealloyed powder obtained by EIGA presents different microstructures depending on the particle size and it is mainly composed by α-metastable phase. A phase transformation occurs in the temperature range of 600 ºC-750 ºC transforming from α to $\alpha_2+\gamma$ phases.
2. γ-TiAl intermetallic alloy can be successfully consolidated at temperatures equal or higher than 1000 ºC developing duplex and lamellar microstructures. If the processing temperature is below 1000 ^{o}C, there is a formation of Al_3Ti phase at the particle boundaries, which is deleterious to the room temperature and high temperature mechanical properties.
3. A compressive yield strength values of 1050, 655 and 626 MPa were achieved for duplex, nearly lamellar and fully lamellar microstructures respectively at room temperatures. Whereas at 750 ^{o}C the nearly lamellar and fully lamellar microstructures exhibit 440 and 425 MPa yield strength values. These excellent values are due to the refinement of the microstructure and its microconstituents.
4. Differences in between the reduced elastic modulus of grains and colonies in a duplex microstructure suggest that a higher volume fraction of γ phase can be associated to the grains while a higher volume fraction of α_2 phase can be associated to the colonies.

5. ACKNOWLEDGEMENTS

Funding from the Spanish Ministry of Science and Innovation through projects MAT2009-14547-C02-01 and MAT2009-14547-C02-02 is acknowledged. The Madrid Regional Government partially supported this project through the ESTRUMAT grant (P2009/MAT-1585). The authors would like to thank the Helmholtz-Zentrum für Material und Küstenforschung GmbH (Geesthacht, Germany) for manufacturing γ-TiAl powders. The authors are grateful to Dr. Ilchat Sabirov for his help with the FAHP process in the Gleeble 3800 equipment. Dr. Jon Molina and Mr. Saeid Loftian are sincerely thanked for their assistance in nanoindentation tests.

REFERENCES

1. M. Yamaguchi, H. Inui, H. Ito, Acta Mater. 48 (2000) 307-322.
2. H. Clemens, S. Mayer, Adv. Eng. Mater. 15 (2013) 191-215.
3. D. M. Dimiduk, Mat. Sci. Eng. A 263 (1999) 281-288.
4. K. Kothari, R. Radhakrishnan, N.M. Wereley, Progress in Aerospace Sciences 55 (2012)1-16.
5. M.E. Kassner, M.T. Pérez-Prado, Fundamentals of creep in metals and alloys. Elsevier, Oxford, UK, 2004.
6. T.A. Parthasarathy, P.R. Subramanian, M.G. Mendiratta, D.M. Dimiduk DM, Acta Mater. 48 (2000) 541-551.
7. H. Zhu, D. Seo, K. Maruyama. Mater. Trans. 45 (2004) 2618-2621.
8. S.C. Huang, E.L. Hall, Metall. Trans. 22 (1991) 427-439.
9. F. Appel, J.D. Paul, M. Oehring. γ-Titanium Aluminides. Wiley-VCH, 2011.
10. C. Choi, Y.T. Lee, C.S. Lee, Scripta Mater. 36 (1997) 821-827.
11. S.C. Huang. Structural intermetallics eds. R. Darolia, J.J. Lewandowski, C.T. Liu, P.L. Martin, D.B. Miracle and M.V. Nathal, TMS, Warrendale, PA, 299.
12. R.M. Imayev, V.M. Imayev, T.G. Khismatullin, M. Oehring, F. Appel, Rev. Adv. Mater. Sci. 11 (2006) 99-108.

13. Y.W. Kim, Intermetallics 6 (1998) 623-628.
14. H.A. Calderon, V. Garibay-Febles, M. Umemoto, M. Yamaguchi, Mat. Sci. Eng. A 329-331 (2002) 196-205.
15. M. Thomas, J.L. Raviart, F. Popoff, Intermetallics 13 (2005) 944-951.
16. L. Cheng, H. Chang, B. Tang, H. Kou, J. Li , J. Alloy Compd. 552 (2013) 363-369.
17. Y.H. Wang, J.P. Lin, X.J. Xu, Y.H. He, Y.L. Wang, G.L. Chen GL, J. Alloy. Compd. 458 (2008) 313-317.
18. X.J. Xu, J. P. Lin, Y.L. Wang, J.F. Gao, Z. Lin, G.L. Chen, J. Alloy. Compd. 414 (2006) 175-180.
19. K. Matsugi, N. Ishibashi, T. Hatayama, O. Yanagisawa, Intermetallics 4 (1996) 457-467.
20. Y. Liu, B. Huang, Y. He, K. Zhou, J. Mater. Sci. Technol. 16 (2000) 605-610.
21. E. Schwaighofer, H. Clemens, S. Mayer, J. Lindemann, J. Klose, W. Smarsly, V. Guther, Intermetallics 44 (2014) 128-140.
22. R. Gerling, H. Clemens, F.P. Schimasky, Adv. Eng. Mater. 6 (2004) 23-37.
23. S. Grasso, Y. Sakka, G. Marizza, Sci. Technol. Adv. Mater. 10 (2009) 1-24.
24. M.S. Yurlova, V.D. Demenyuk, L.Y. Lebedeva, D.V. Dudina, E.G. Grigoryev, E.A. Olevsky, J. Mater. Sci. 49 (2014) 952-985.
25. G. Molenat, L. Durand, J. Galy, A. Couret, J. Metall. (2010) Article ID 145431.
26. H. Jabbar, A. Couret, L. Durand, J.P. Monchoux, J Alloy. Compd. 509 (2011) 9826-9835.
27. K. Kothari, R. Radhakrishnan, N.M. Wereley, T.S. Sudarshan, Powder Metall. 50 (2007) 21-27.
28. G. Molenat, M. Thomas, J. Galy, A. Couret, Adv. Eng. Mater. 9 (2007) 667-669.
29. A. Couret, G. Molenat, J. Galy, M. Thomas, Intermetallics 16 (2008) 1134-1141.
30. H. Jabbar, J.P. Monchoux, F. Houdellier, M. Dolle, F.P. Schimansky, F. Pyczak, M. Thomas, A. Couret , Intermetallics 18 (2010) 2312-2321.
31. H. Jabbar, J.P. Monchoux, M. Thomas, A. Couret, Acta Mater. 59 (2011) 7574-7585.

32. Y. Huang, Y. Wang, H. Fan, J. Shen, Intermetallics 31 (2012) 202-207.
33. J. Guyon, A. Hazotte, J.P. Monchoux, E. Bouzy , Intermetallics 34 (2013) 94-100.
34. M.A. Lagos, I. Agote, Intermetallics 36 (2013) 51-56.
35. X. Shulong, X. Lijuan, Y. Hongbao, C. Yuyong, Rare Metal Materials and Engineering 42 (2013) 23-27.
36. H. Jabbar, J.P. Monchoux, M. Thomas, F. Pyczak, Intermetallics 46 (2014) 1-3.
37. M. Hohman, N. Ludwig, German Patent DE 4102 101 A1 (1991).
38. R. Muñoz-Moreno, B. Srinivasarao, I. Sabirov, E.M. Ruiz Navas, J.M. Torralba EuroPM12-non ferrous Symp. Proc. (2012).
39. T. Mishin, C. Herzig, Acta Mater. 48 (2000) 589-623.
40. V. Raghavan, Phase Diagrams Evaluation - Section II 32 (2011) 465-467.
41. V. Raghavan, Phase Diagrams Evaluation - Section II 33 (2012) 143-144.
42. D.E. Larsen, S. Kampe, L. Christodoulou, Mater. Res. Soc. Symp. Proc. 194 (1990) 285-292.
43. C. Yang, D. Hu, A. Huang, M. Dixon, Intermetallics 32(2013) 64-71.
44. J.J. Valencia, C. McCullough, C.G. Levi, R. Mehrabian, Acta Metall. 37 (1989) 2517-2530.
45. T. Voisin, L. Durand, N. Karnatak, S. Le Gallet, M. Thomas, Y. Le Berre, J.F. Castagné, A. Couret, J. Mater. Process. Tech. 213 (2013) 269-278.
46. A. Denquin, S. Naka, Acta Mater. 44 (1996) 343-352.
47. S. Zghal, M. Thomas, S. Naka, A. Finel, A. Couret, Acta Mater. 53 (2005) 2653-2664.
48. A. Denquin, S. Naka, Acta Mater. 44 (1996) 353-365.
49. J.S. Luo, T. Voisin, J.P. Monchoux, Intermetallics 36 (2013) 12-20.
50. D.Y. Seo, L. Zhao, J. Beddoes, Mat. Sci. Eng. A 329-331 (2002) 130-140.
51. Y. Chen, H. Niu, F. Kong, S. Xiao, Intermetallics 19 (2011) 1405-1410.
52. S. Biamino, A. Penna, U. Ackelid, S. Sabbadini, O. Tassa, P. Fino, M. Pavese, P. Gennaro, C. Badini, Intermetallics 19 (2011) 776-781.
53. C.Yang, D. Hu, X. Wu, A. Huang, M. Dixon, Mat. Sci. Eng. A 534 (2012) 268-275.

54. T.T. Sasaki, T. Mukai, K. Hono, Scripta Mater. 57 (2007) 189-192.

55. B. Srinivasarao, K. Oh-ishi, T. Ohkubo, T. Mukai, T. Hono, Scripta Mater. 58 (2008) 759-762.

56. L. Cheng, H. Chang, B. Tang, H. Kou, J. Li, J. Alloy. Compd. 552 (2013) 363-369.

FIGURE CAPTIONS

Fig. 1 (a) Powder particle size distribution and (b-e) backscattered (BSE) SEM micrographs showing the prealloyed powder microstructures for different particle's size: (a) 30 μm diameter and (b) 120 μm diameter; (c, d) single phase regions present in particles of different sizes

Fig. 2 XRD patterns of prealloyed Ti-45Al-2 Nb-2 Mn-0.8vol.%TiB_2 powder at 25 ºC, 600 ºC, 800 ºC and 1000 ºC

Fig. 3 DTA analysis comparing the powder and the centrifugally cast Ti-45Al-2Nb-2Mn (at.%)-0.8vol.%TiB_2 alloy showing different thermal behavior at 600 ºC – 750 ºC

Fig. 4 BSE SEM micrographs (a) at low and (b) high magnification of the powder heated at 800 ºC.

Fig. 5 Typical evolution of the temperature and displacement versus time recorded in-situ during the FAHP processing at (a) 900 ºC and at (b) 1000 ºC during 10 minutes

Fig. 6 XRD patterns of FAHP1, FAHP2, FAHP3, FAHP4 and FAHP5 materials exhibiting $\alpha_2+\gamma$ peaks.

Fig. 7 BSE SEM micrographs showing the microstructure of the FAHP1 consolidated sample: (a-b) duplex microstructure in the center of the sample, (c) not completely sintered edge area and (d) Al_3Ti phase boundary area between the powder particles of FAHP1 sample.

Fig. 8 BSE SEM micrographs showing the duplex microstructure of the FAHP2 consolidated sample (a) with signs of former powder particles and (b) a combination of lamellar colonies and equiaxed grains.

Fig. 9 BSE SEM micrographs showing the FAHP3 (a, b) nearly lamellar microstructure in the center of the sample and (c) the gradient in the microstructure along the sample's edges

Fig. 10 BSE SEM micrographs showing the FAHP4 (a-b) nearly lamellar microstructure along the whole of the sample and (c) edges areas with an increasing of the equiaxed grains volume fraction; FAHP5 (d, e) fully lamellar microstructure

Fig. 11 TEM micrograph of the FAHP4 sample showing a fine lamellar colony

Fig. 12 Compression tests stress-strain curves at (a) room temperature and (b) high temperature (750 ºC) conditions for FAHP2, FAHP4 and FAHP5 materials. X indicates that the test is stopped

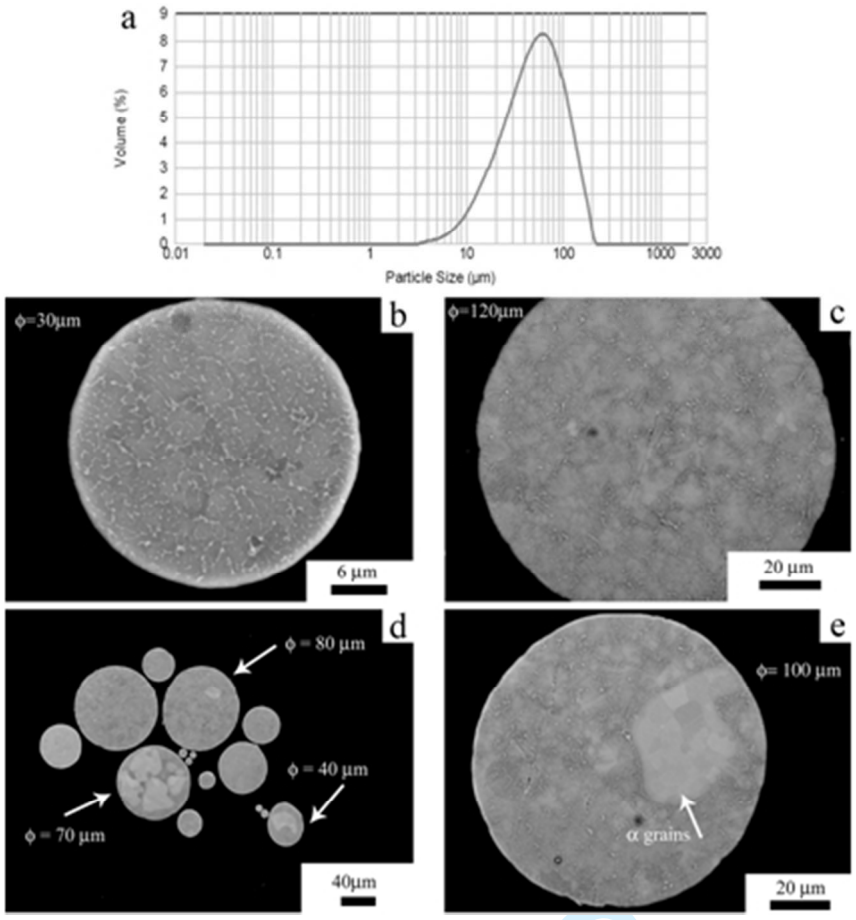

153x160mm (72 x 72 DPI)

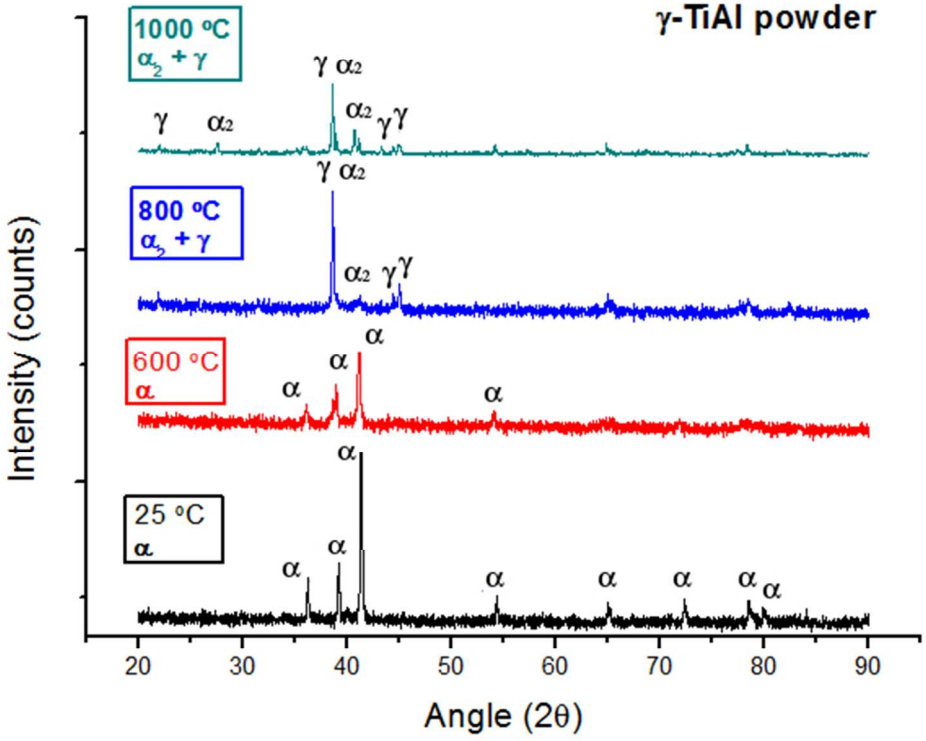

216x170mm (72 x 72 DPI)

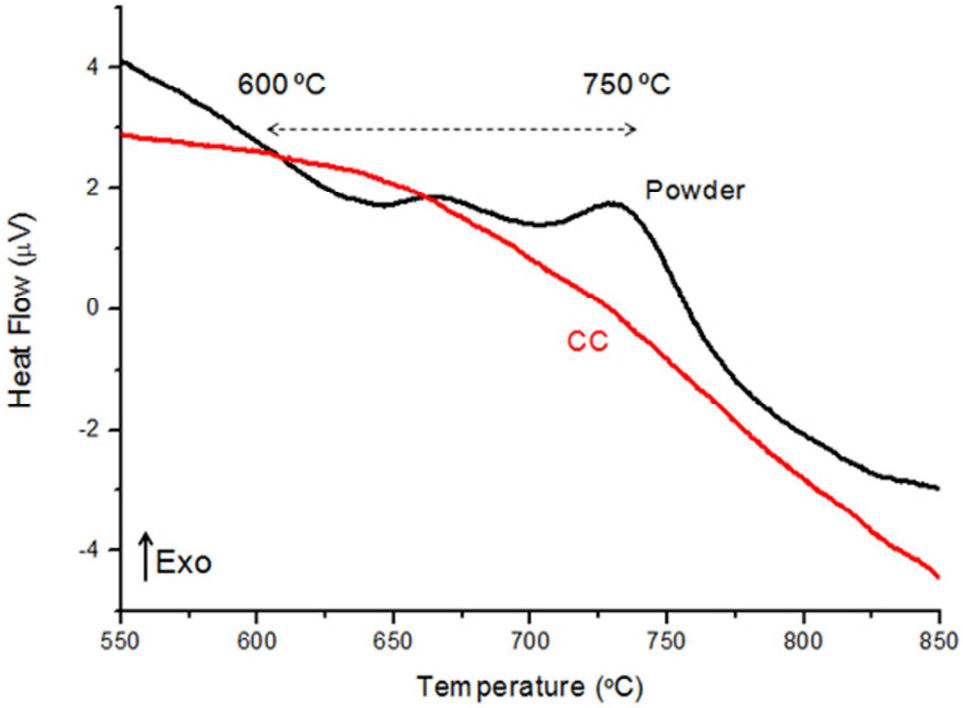

200x147mm (72 x 72 DPI)

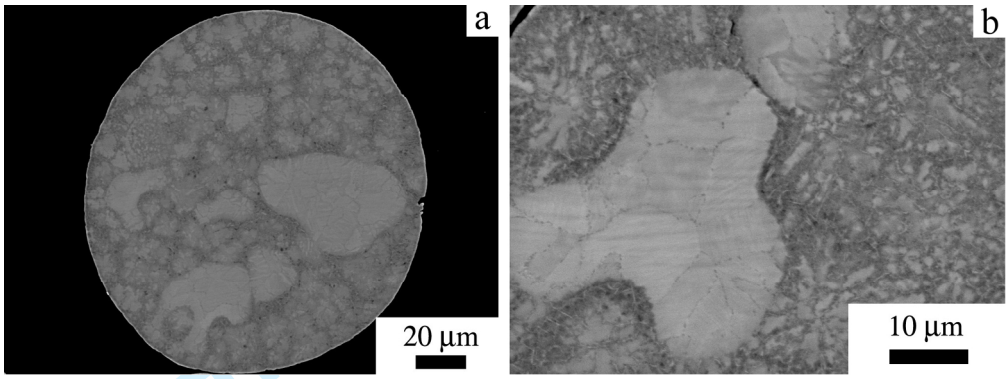

288x106mm (182 x 182 DPI)

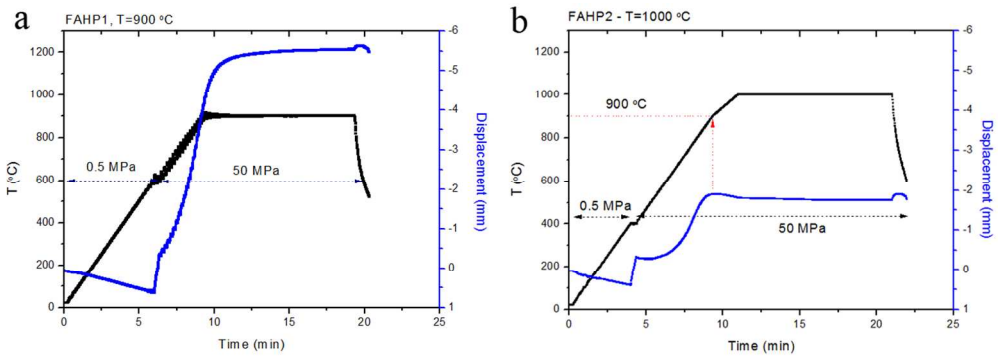

472x168mm (72 x 72 DPI)

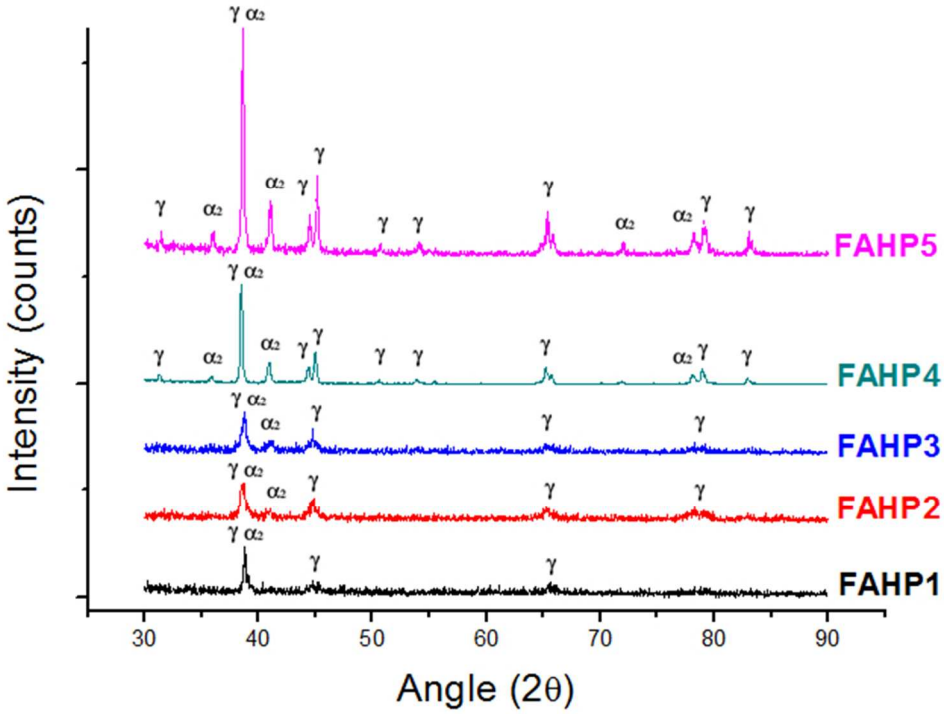

233x173mm (72 x 72 DPI)

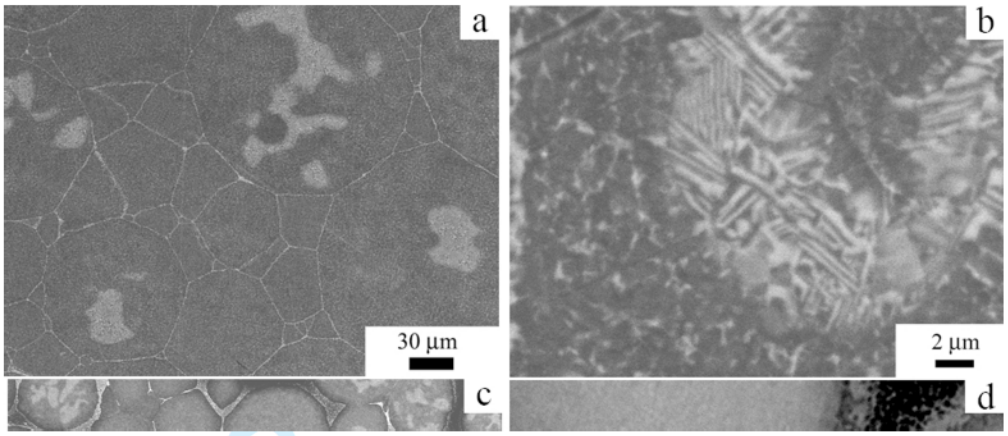

348x259mm (75 x 75 DPI)

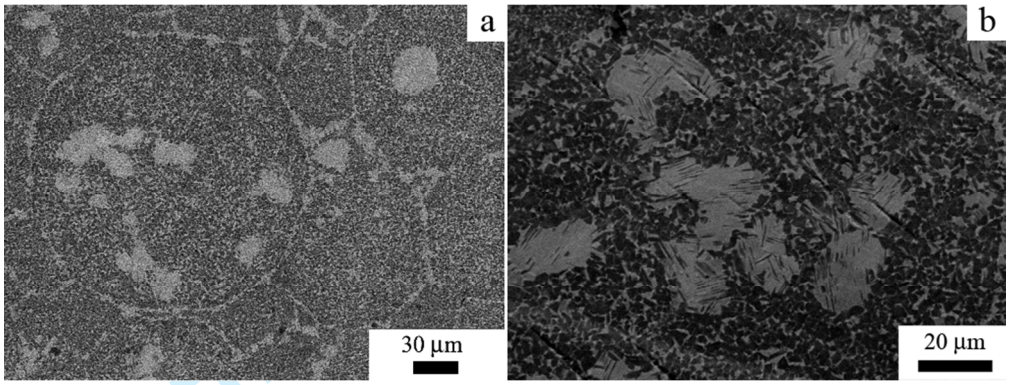

359x135mm (72 x 72 DPI)

361x272mm (72 x 72 DPI)

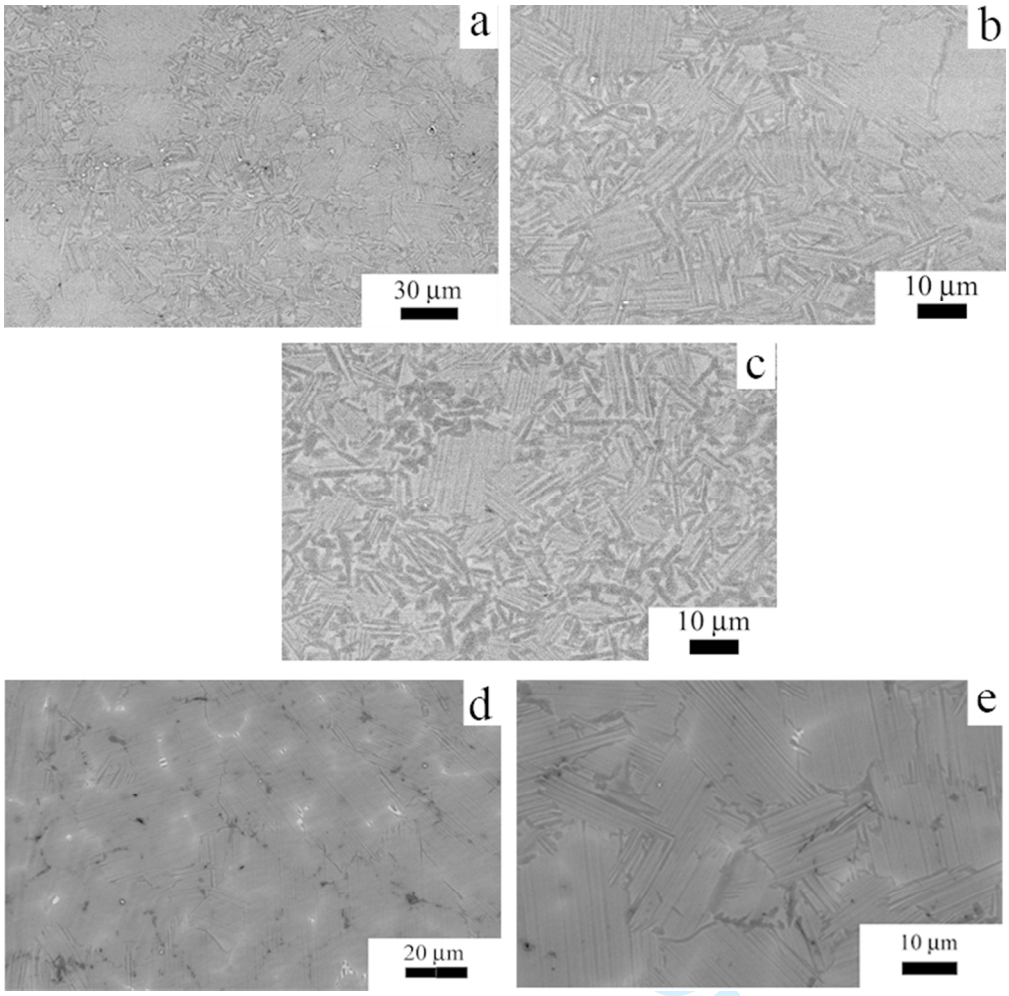

264x260mm (75 x 75 DPI)

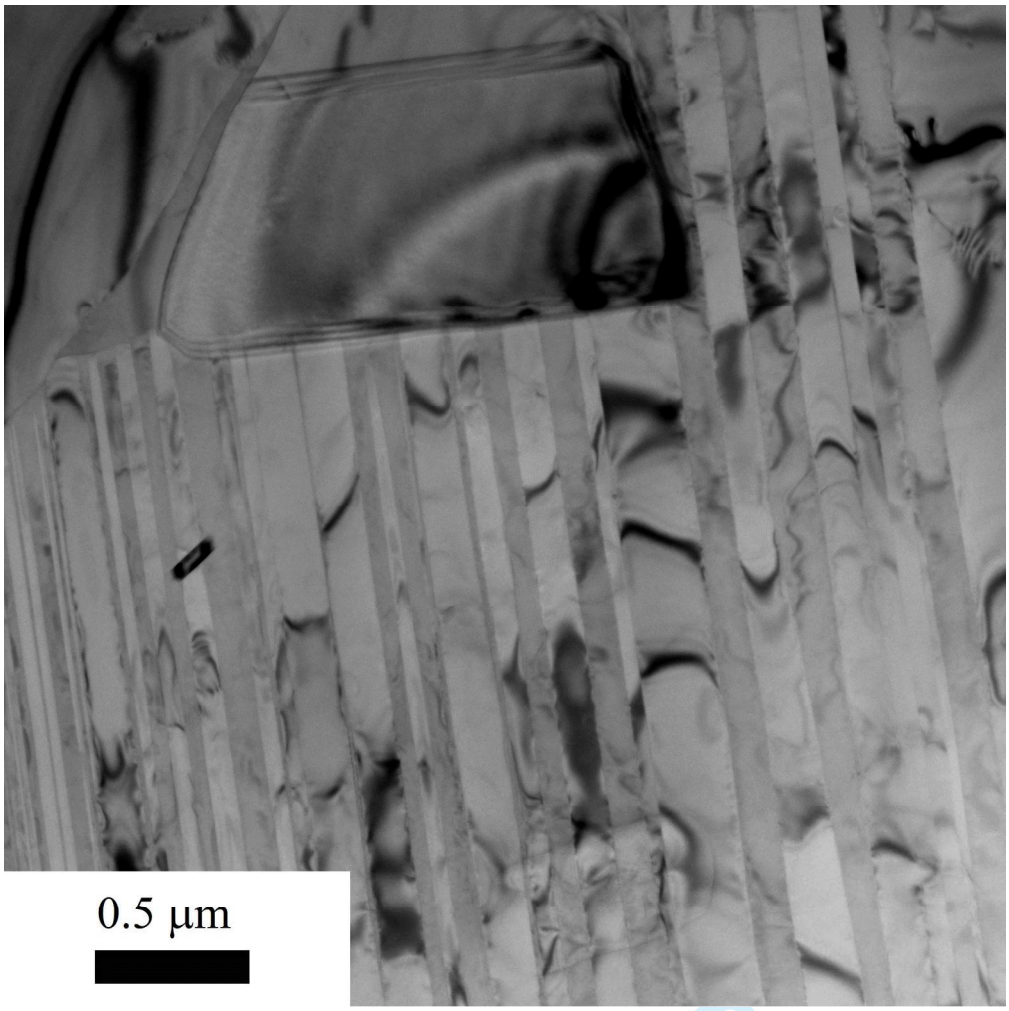

722x722mm (72 x 72 DPI)

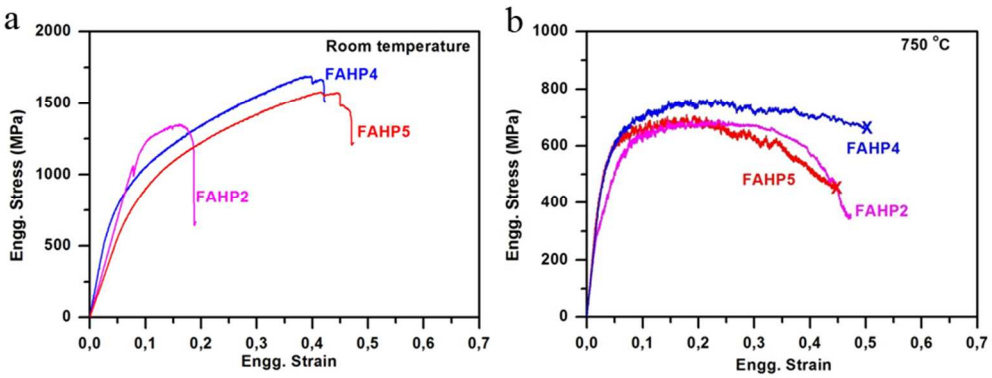

349x135mm (72 x 72 DPI)

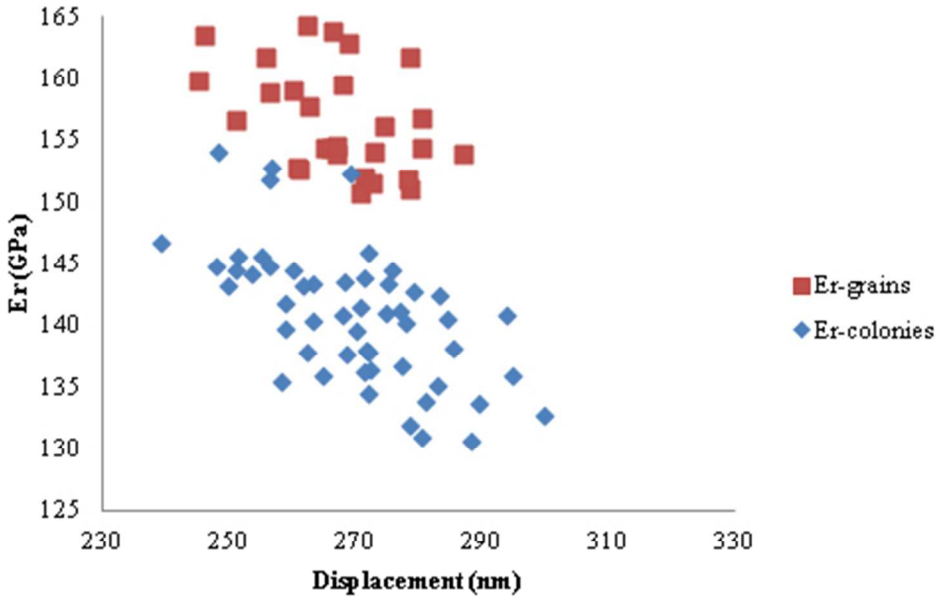

178x116mm (72 x 72 DPI)